Insights from ScS–S measurements on deep mantle attenuation

S. Durand [a,*], J. Matas [a], S. Ford [b], Y. Ricard [a], B. Romanowicz [c,d,e], J.-P. Montagner [d]

[a] Laboratoire de Géologie de Lyon-Terre Planète Environnement, CNRS UMR5570, École Normale Supérieure de Lyon, Université de Lyon, Université Claude Bernard Lyon 1, 46 Allée d'Italie, 69364 Lyon Cedex 07, France
[b] Ground-based Nuclear Detonation Detection Programs, Lawrence Livermore National Laboratory, Livermore, CA 94550, USA
[c] Collège de France, Paris, France
[d] Institut de Physique du Globe de Paris, Université Paris-Diderot, 1 rue Jussieu, 75238 Paris Cedex 05, France
[e] Berkeley Seismological Laboratory, 209 McCone Hall, Berkeley, CA 94720-4760, USA

ARTICLE INFO

ABSTRACT

We apply a recently developed method based on the instantaneous frequency to analyze broadband seismic data recorded by the transportable USArray. We measure in the frequency band [0.018–0.2] Hz about 700 high-quality differential ScS–S anelastic delay times, $\delta t^{\star}_{ScS-S}$, sampling the mantle below Central America and below Alaska that we compare to elastic delay times, δt_{ScS-S}, obtained by cross-correlating the S and ScS signals. We confirm that the instantaneous frequency matching method is more robust than the classical spectral ratio method. By a series of careful analyses of the effects of signal-to-noise ratio, source mechanism characteristics and possible phase interferences on measurements of differential anelastic delay times, we demonstrate that in order to obtain accurate values of δt^{*}_{ScS-S} the seismic records must be rigorously selected. In spite of the limited number of data that satisfy our quality criteria, we recover, using an additional stacking procedure, a clear dependence of δt^{*}_{ScS-S} on the epicentral distance in the two regions. The absence of correlation between the obtained anelastic and elastic delay-times indicates a complex compositional-thermal origin of the attenuation structure, or effects of scattering by small scale structure, in accordance with possible presence of subducted material. The regional 1-D inversions of our measurements indicate a non-uniform lower mantle attenuation structure: a zone with high attenuation in the mid-lower mantle ($Q_\mu \approx 250$) and a low attenuation layer at its base ($Q_\mu \approx 450$). A comparison of our results with low-frequency normal-model Q models is consistent with frequency-dependent attenuation with $Q_\mu \propto \omega^\alpha$ and $\alpha = 0.1$–0.2 (i.e. less attenuation at higher frequencies), although possible effects of lateral variations in Q in the deep mantle add some uncertainty to these values.

1. Introduction

Tomographic images of the mantle reveal the presence of heterogeneities of various wavelengths. However, their interpretation in terms of temperature, chemical or petrological anomalies remains challenging (e.g. Masters et al., 2000; Trampert et al., 2004; Ricard et al., 2005). The difficulty comes from the fact that the properties of the mantle mineralogical phases are not yet accurately known at relevant pressure and temperature conditions. Another complexity comes from the non-uniqueness of the interpretations. For example, increasing the iron content or the temperature has similar effects on seismic velocities. Together with the elastic parameters, the intrinsic seismic attenuation of the mantle is a key observation for understanding mantle structure (e.g. Karato and Karki, 2001; Matas and Bukowinski, 2007). Indeed, seismic attenuation is sensitive to both temperature and composition but in a way different than seismic

velocity (e.g. Jackson and Anderson, 1970; Karato and Spetzler, 1990). Therefore, coupling elastic and anelastic models should help to disentangle the thermal and compositional components of mantle heterogeneities.

In the last three decades, several shear attenuation profiles, expressed in terms of quality factor Q_μ, were obtained from normal modes and/or surface wave attenuation measurements (Anderson, 1980; Dziewonski and Anderson, 1981; Widmer et al., 1991; Durek and Ekström, 1995, 1996; Resovsky et al., 2005). Depending on the data and on the parameterization, the resulting radial Q_μ profiles differ by 30% in the lower mantle (see reviews by Romanowicz and Durek, 2000; Romanowicz and Mitchell, 2007). In order to add new constraints on the lower mantle, Lawrence and Wysession (2006a) measured ≈ 30,000 differential ScS–S attenuation values and Hwang and Ritsema (2011) ≈ 150,000 P and S spectral ratios. Even though both studies are at the global scale, they obtain different shear attenuation profiles. While Lawrence and Wysession (2006a) predict an attenuation profile with a minimum quality factor Q_μ of ≈200 around 1500 km depth and a maximum of ≈500 near the CMB, Hwang and Ritsema (2011) find a continuous decrease of attenuation

* Corresponding author. Tel.: +33 472448377.
E-mail address: stephanie.durand@ens-lyon.fr (S. Durand).

from the top of the lower mantle ($Q_\mu \approx 300$) to the bottom ($Q_\mu \approx 600$). This disagreement may come from the difference in methods between these two studies or from the fact that their measurements sample different regions of the deep mantle. It can also be due to the effect on the measurements of scattering and focusing/defocusing from the 3-D elastic structure, which can be important when using body waves. Indeed, complicated data processing, uneven data coverage, phase interferences, and effects related to the 3-D elastic structure make body wave attenuation measurements challenging.

The aim of this study is to bring new insights on the origin of deep mantle heterogeneities, using high quality ScS–S attenuation measurements. These measurements can be done either in the time domain (Chan and Der, 1988) or in the frequency domain. However, Bhattacharyya (1998) has shown that the latter methods are more robust and less sensitive to phase interference and to noise. Therefore, spectral ratio (SR) methods are usually applied for the measurement of differential ScS–S attenuation. There exist several variants of SR methods: most authors apply a spectral stacking with both phase and amplitude information (Jordan and Sipkin, 1977; Sipkin and Jordan, 1980; Lay and Wallace, 1983; Sipkin and Revenaugh, 1994; Suetsugu, 2001), while Nakanishi (1979) uses a maximum likelihood algorithm. In contrast to these previous SR studies, we adopt a new method, the Instantaneous Frequency Matching (IFM) method, developed by Matheney and Nowack (1995). The IFM method was recently applied by Ford et al. (2012) who showed that the IFM (based on phase analysis) better performs than SR (based on amplitudes analysis) when encountering the usual problems of body wave attenuation measurements (low signal-to-noise ratios, phase windowing). In a nutshell, the phase is indeed a more robust signal than the amplitude, because the phase obeys a minimization principle, Fermat's principle, whereas no such principle exists for the amplitude.

We first apply the IFM method on synthetic seismograms in order to test its accuracy and sensitivity to the source mechanism and to interfering phases. Second, we analyze ≈700 carefully selected broadband data recorded by the USArray in order to evaluate and analyze the radial and lateral variations of shear attenuation in the deep mantle. Finally, we run the IFM method on stacks of seismograms to derive a radial profile of shear attenuation.

2. The instantaneous frequency matching method

When a seismic wave propagates in an attenuating medium, its amplitude decreases and its frequency content is dispersed. The attenuation of the signal (here an S wave) is quantified by the anelastic delay time t^* defined as

$$t^* = \int_{\text{path}} \frac{ds}{\beta Q_\mu} \tag{1}$$

where β is the S velocity, Q_μ the S wave quality factor, and s the abscissa along the ray. The loss of amplitude due to intrinsic attenuation at angular frequency ω is

$$\exp\left(-t^* \frac{\omega}{2}\right),$$

and the dispersion of the signal due to attenuation is

$$\exp\left(it^* \frac{\omega}{\pi} \ln\left(\frac{\omega}{\omega_r}\right)\right),$$

where ω_r is a reference frequency, often chosen to be 1 Hz. This expression of the dispersion is only valid for a frequency independent attenuation. Although Lekic et al. (2009) and Zaroli et al. (2010) have recently quantified the weak frequency dependence of attenuation, using a frequency independent attenuation is an acceptable approximation in this study where the range of frequencies of the signal is rather narrow around the reference frequency ω_r of 1 Hz.

The IFM method transforms the seismic trace into two ancillary signals: the instantaneous amplitude and frequency. They are obtained by classical complex trace analysis (Taner et al., 1979) involving the conjugate of the real data, its Hilbert transform (for details see Matheney and Nowack, 1995). The maxima of the amplitudes define the arrivals of the different seismic phases. At each maximum, the time derivative of the instantaneous phase defines an instantaneous frequency. The IFM method assumes that the radiation patterns of the S and ScS waves are similar and that the signals are not contaminated by noise or by other seismic phases. In this case and considering only horizontally polarized SH waves, so that the ScS is simply reflected at the CMB, the difference between the two waveforms is only due to a difference in the intrinsic attenuation along the two paths (we discuss later the corrections that the presence of seismic anisotropy may require). The differential anelastic delay time ScS–S, denoted $\delta t^\star_{ScS-S}$, is therefore obtained by matching the instantaneous frequencies of the direct S and core-reflected ScS seismic waves (Ford et al., 2012). This is done by applying the so-called "causal attenuation operator" (Aki and Richards, 1980; Müller, 1983) defined as

$$D(\omega) = \exp\left(-\frac{\omega}{2}\delta t^*_{ScS-S}\left(1 - \frac{2i}{\pi}\ln\frac{\omega}{\omega_r}\right)\right) \tag{2}$$

on the S wave until its instantaneous frequency becomes equal to that of the ScS.

The procedure is illustrated in Fig. 1 (see also Ford et al., 2012). The first step is to compute the envelope of the signal in order to pick the arrival times of the seismic phases (Fig. 1, middle panel, black vertical lines). Then we compute the instantaneous frequency and compare its value at the arrival times of the two waves in the time domain. The amplitude of the S wave is then attenuated using $D(\omega)$, in the frequency domain, for various $\delta t^\star_{ScS-S}$ until the instantaneous frequencies of the S and ScS match.
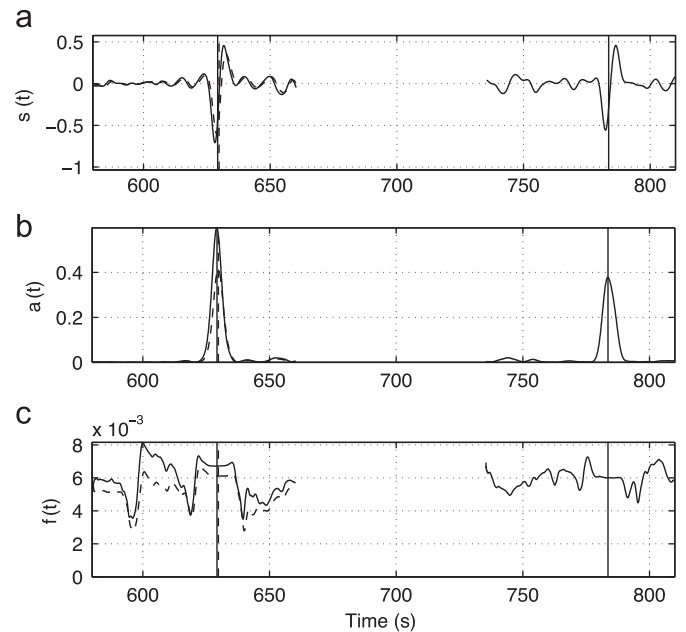

Fig. 1. Instantaneous frequency matching (IFM) method. First, we pick the S and ScS seismic phases by taking the maximum of the envelope (middle panel). Then we compute the instantaneous frequency and compare its value in the time domain at the arrival times of the two seismic waves. The S wave is attenuated using the causal operator $D(\omega)$, Eq. (2), in the frequency domain for a range of $\delta t^\star_{ScS-S}$ until the instantaneous frequencies are matched in the time domain. The dashed lines correspond to the attenuated seismogram, amplitude and instantaneous frequency. The $\delta t^\star_{ScS-S}$ in this example is 0.6 s. (a) Filtered [0.018 0.2] Hz and anisotropy corrected seismograms, (b) envelope and (c) instantaneous frequency (Hz).

3. Synthetic tests and data selection

We first carefully benchmark the IFM method to determine its range of applicability and to compare its accuracy with the SR method. By computing synthetic seismograms using PREM (Dziewonski and Anderson, 1981) and a reflectivity code (Fuchs and Müller, 1971; Müller, 1985), we evaluate the effects of interfering phases and of the source-radiation pattern on the measurements. We consider a deep event (depth 600 km), a source with strike, dip, rake angles of $0°$, $30°$ and $90°$, respectively, and azimuths (with respect to the radiation pattern) of $\phi = 0°$ and $\phi = 20°$.

Partial travel time curves of the synthetic seismograms are presented in Fig. 2. The arrival times of the waves are independent of the azimuth (left panel) and the figure focuses on the S wave (left panel, black line) and the ScS wave (left panel, dashed line). Fig. 2 illustrates that interference occurs between the ScS, SS and sS around $45°$ and between the ScS and s410S around $65°$. In the case of anisotropy, other interferences may happen. For example, the SKS signal on the transverse component may interfere with the ScS around $60°$ of epicentral distance for a deep event. We also plot the seismic signal for different azimuths ϕ (top right panel for $\phi = 0°$, bottom right panel for $\phi = 20°$). It can be noted that for the chosen radiation pattern, the amplitude of the S wave decreases with increasing azimuth and consequently decreases the signal-to-noise ratio of an ScS–S analysis.

In Fig. 3 (top panel) we present the $\delta t^\star_{ScS-S}$ measurements obtained from our synthetic seismograms using the IFM method. We show the effect of the radiation pattern by changing the path azimuth ϕ from $0°$ (black dots) to $20°$ (red dots). For the epicentral distances used in this study, the difference in radiation pattern between the S and ScS is minimal when $\phi = 0°$ and increases with ϕ. The effect of the radiation pattern has two origins. First, away from the direction of maximum radiation, the difference in amplitude between the S and ScS is larger and may be partially accounted by the IFM method as intrinsic attenuation. Second, when approaching a source mechanism node, the signal-to-noise ratio is lower which also affects the measurement. Note that the effect of phase interferences for epicentral distances lower than $45°$ as well as that with the s410S around $65°$ clearly prevents us from obtaining a reliable value of the differential anelastic delay

time. We also plot the theoretical $\delta t^\star_{ScS-S}$ (black line) that can be calculated by integrating $1/\beta Q_\mu$ given by PREM along the S and ScS wave paths, using Eq. (2). The comparison illustrates that the accuracy of the IFM method is around 0.05 s. It also shows that interferences affect the measurements by at least 0.1 s.

In order to compare the efficiency of the IFM and SR methods, we show, in Fig. 3 (bottom panel), $\delta t^\star_{ScS-S}$ measured on the synthetic seismograms using the SR method. As was already discussed in Ford et al. (2012), the difficulty with the SR method is related to the choice of the time window over which the phases are isolated (time window of 30 s, circles, and 50 s, diamonds). The results obtained appear to be quite unstable indeed and sensitive to this time window size. Moreover, the measured $\delta t^\star_{ScS-S}$ do not well reproduce the predictions of PREM.

By comparing the two panels, it is obvious that the IFM method provides a more accurate and robust estimate of the anelastic delay time. We also show that one must be very careful with the data selection when applying the IFM method on real seismograms in order to avoid a low signal to noise ratio, the presence of interfering phases and an inappropriate source mechanism. Performing systematic synthetic tests appears to be the best way to rigorously and objectively select the data.

In conclusion, in our study we use the following procedure to select seismic data recorded by the transportable USArray. We first pre-select all the events with magnitude between 5.9 and 6.9 (in order to avoid complex source–time functions), deeper than 100 km (in order to limit the effects of the crust) and epicentral distance in the range $40–70°$. For too shallow earthquakes the interferences between the sS, SS and S make the method unreliable. At distances smaller than $40°$, there are triplications that complicate the S signals, and at distances larger than $70°$, the S and the ScS cannot be separated. Because of the geographical location of the USArray and the constraints on the epicentral distances, we can only use seismic paths sampling the mantle below Alaska and Central America. Only a limited number of earthquakes have an appropriate radiation pattern. We then compute the synthetic seismograms corresponding to the observed data, run the IFM method on them and exclude all data for which the synthetic test shows evidence of interfering phases or of a source effect. The final dataset is presented in Fig. 4. We end up with 3 major events: 2 of them sampling Central America and 1 sampling
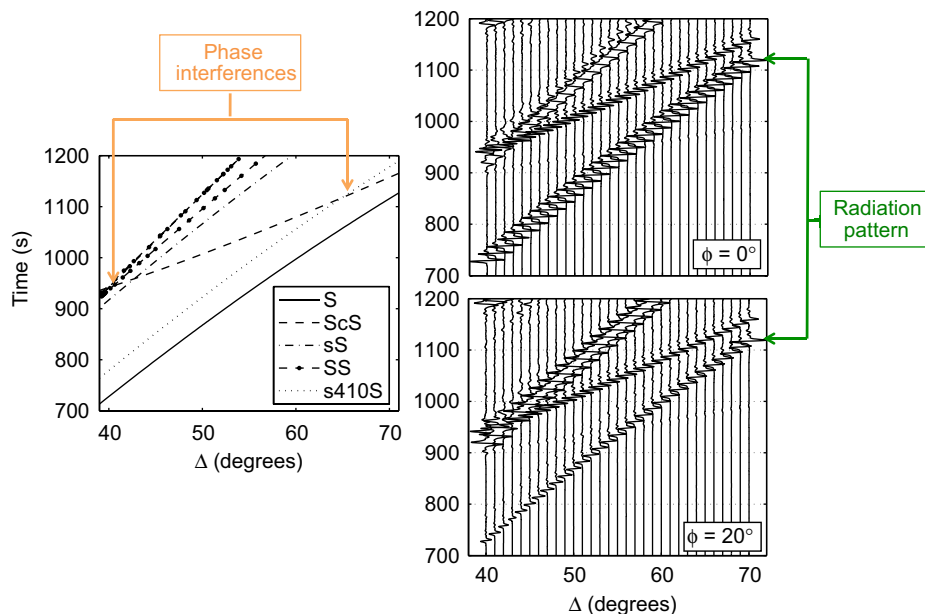

Fig. 2. Hodochrons of the synthetic seismograms. Two simulations for an event depth of 600 km, strike $= 0°$, dip $= 30°$ and rake $= 90°$ and two path azimuths $\phi = \{0, 20\}°$ are shown. (left) Phases are interfering around $45°$ (ScS, sS, SS) and around $65°$ (ScS, s410S). (right) The change in path azimuth causes a significant decrease of the S amplitudes.
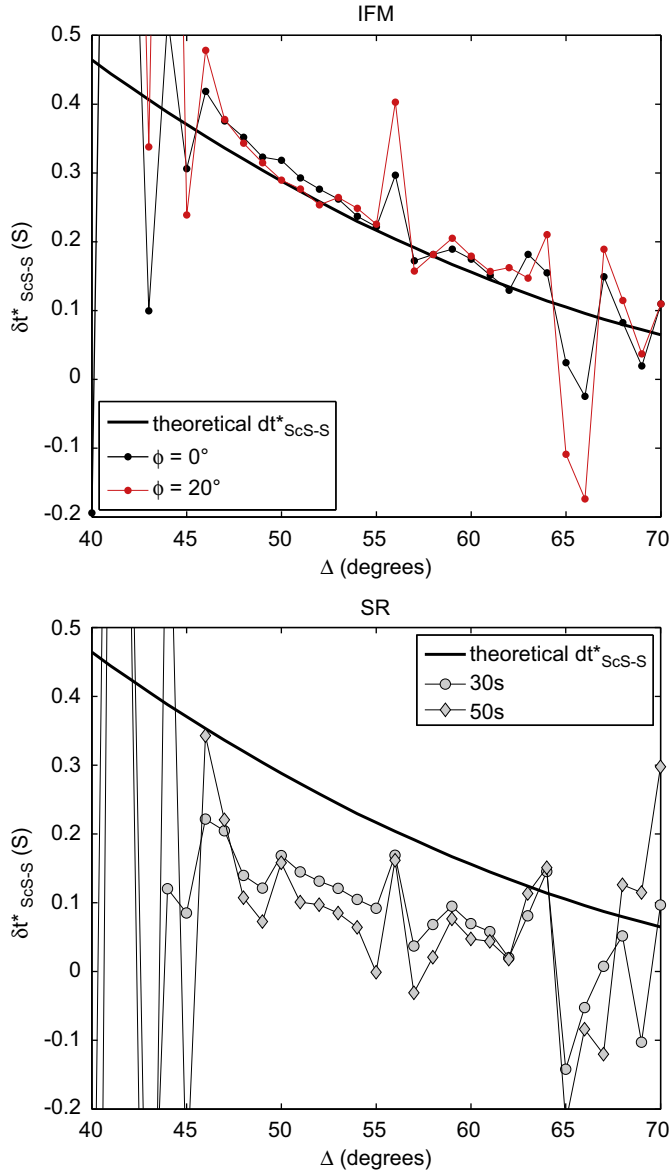
Fig. 3. Comparison of the SR and IFM methods. (top) Differential anelastic delay times $\delta t^\star_{ScS-S}$ obtained by the IFM method applied on the synthetic seismograms plotted in Fig. 2 for path azimuths ϕ of 0° (black dots) and 20° (red dots). (bottom) Differential anelastic delay times $\delta t^\star_{ScS-S}$ obtained by the SR method applied on the set of synthetic seismograms with $\phi = 0°$ for two time windows, 30 s (circles) and 50 s (diamonds). The comparison of the results highlights the better accuracy of the measurements obtained with the IFM method. The two plots also illustrate the effect of interfering phases and of radiation pattern on the measurements. The presence of interfering phases around 45° and 65° significantly degrades the measurements, while the effect of the azimuth is negligible except when phases are interfering. The theoretical values of $\delta t^\star_{ScS-S}$ obtained using PREM parameters and Eq. (2) are plotted as black curve. (For interpretation of the references to color in this figure caption, the reader is referred to the web version of this article.)

Alaska. This choice still corresponds to ≈700 seismograms recorded on the dense USArray network. Although it may seem a small number compared to the tens of thousand automatic measurements of Lawrence and Wysession (2006a) or Hwang and Ritsema (2011), we believe that our careful selection retrieves more meaningful constraints on the origin of the lower mantle heterogeneities in the sampled regions.

For further improvement of our measurements we also correct our observations from anisotropy that may be present under the stations and has been observed in the lowermost mantle of the Caribbean region (Kendall and Silver, 1996; Nowacki et al., 2010).

Anisotropy may affect our observations by coupling SH and SV components. To remove these potential biases, we performed a particle motion analysis to find the splitting parameters (split time dt and fast azimuth ϕ) that best linearized the particle motions of the S and ScS arrivals (Silver and Chan, 1991; Wüstefeld et al., 2008). We then use these values to rotate the traces to the fast axis direction, time-shift them by $-dt$, then rotate the traces back to the transverse direction. By this additional analysis, we indeed detect some anisotropy in our SH observations revealed by elliptical particle motions that lead to $\delta t^\star_{ScS-S}$ corrections of order 0.3 s for Central America and 0.5 s for the North Pacific. These results are similar to those of Ford et al. (2012) who found an anisotropy correction of around 0.25 s on average for their Central America data.

4. Lateral variations of $\delta t^\star_{ScS-S}$

We now run the IFM method on the selected data corrected from anisotropy to measure the $\delta t^\star_{ScS-S}$. In Fig. 5 (left column), we plot their values at the core-reflection points corresponding to the two geographical zones shown in Fig. 4. Remember that the $\delta t^\star_{ScS-S}$ values correspond to a difference of two path integrals. They are not related by any simple way to a local property and it is therefore arbitrary to plot the values of $\delta t^\star_{ScS-S}$ on the core–mantle boundary. These values carry information simultaneously on possible departures from the radial Q_μ profile and on possible presence of lateral variations of attenuation along the paths. In this figure, contributions due to the 1-D attenuation structure given by PREM and the 3-D long wavelength elastic structure given by SAW24B16 (Mégnin and Romanowicz, 2000) have been subtracted. In the PREM Q_μ model, the $\delta t^\star_{ScS-S}$ are positive, decreasing from ≈0.3 s to zero when the epicentral distance increases from 40° to 70° (see Fig. 3, black curve) just because the ScS path is longer than that of the S. The influence of the elastic structure, 1-D or 3-D, on the computed $\delta t^\star_{ScS-S}$ is very weak as the amplitudes of the velocity anomalies are negligible compared to those of the quality factor. Of course, the elastic 3-D structure only accounts for long wavelength heterogeneities. The effect of small scale heterogeneities is difficult to correct and is hopefully averaged out when a significant number of observations are used.

The values of $\delta t^\star_{ScS-S}$ that we measure are highly variable in amplitude and even in sign (the red plus signs denote positive anelastic delay times whereas blue circles correspond to negative ones). Under Central America (top left panel), the $\delta t^\star_{ScS-S}$ values obtained from a deep earthquake range from −3 to 3 s. A similar variability is found in the case of the $\delta t^\star_{ScS-S}$ values obtained for a shallow earthquake (middle left panel). In principle, values obtained independently from deep and shallow earthquakes have no reason to be the same, even when they have the same core reflection point. Under Alaska (bottom left panel), the $\delta t^\star_{ScS-S}$ values also display variations from positive to negative values ranging from −3 to 2 s.

We also plot the $\delta t^\star_{ScS-S}$ (corrected using PREM and SAW24B16) versus epicentral distance (Fig. 5, right column). The associated error bars are defined as the mean of standard deviations of the measurements covering cells of 3° × 3°. Slight trends with the epicentral distance are observed particularly when a moving window averaging is performed (thick grey line). The $\delta t^\star_{ScS-S}$ from 50° to 60° increase for Central America but decrease for Alaska (with large uncertainties especially for Central America). As the two earthquakes have similar depths, these observations cannot be explained by the same radial attenuation structure. The observations suggest a decrease of $\delta t^\star_{ScS-S}$ from 60° to 70° under Central America.
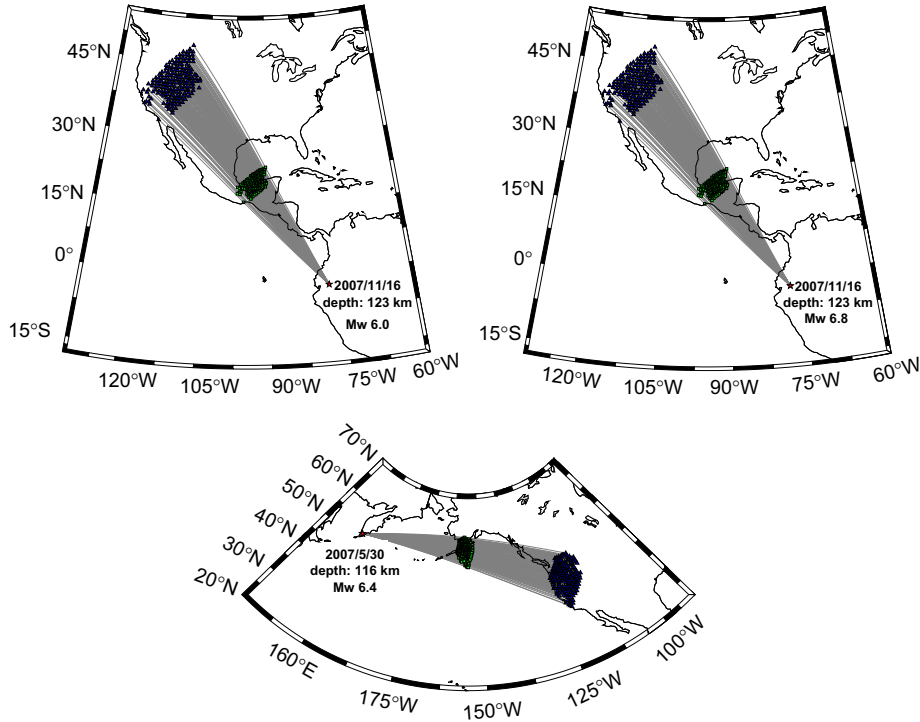
Fig. 4. Selected high quality data recorded by the USArray. (top) Core reflection points under Central America. (bottom) Core reflection points under Alaska. Blue triangles are the stations, red stars the epicenters, green squares the ScS core reflection points and grey lines the seismic paths projected at the surface. (For interpretation of the references to color in this figure caption, the reader is referred to the web version of this article.)

The large amplitudes and the presence of trends with epicentral distance show that the observed $\delta t^{\star}_{ScS-S}$ cannot be explained by the attenuation of PREM. The strikingly rapid changes of $\delta t^{\star}_{ScS-S}$ can be due to intrinsic anelasticity or 3-D elastic effects in a lower mantle that is heterogeneous at very small scales (focusing/ defocusing, scattering or multipathing). The latter are difficult to correct but have been partly quantified at long wavelengths by Ford et al. (2012). They showed, by using the same method, that 3-D elastic heterogeneities cannot account for more than 0.3 s of the measurements.

In order to highlight the long wavelength of the retrieved spatial variations of the $\delta t^{\star}_{ScS-S}$, we run the IFM method on stacks of seismograms. For each event, we first correct the individual signals for the instrument response and for anisotropy, then we stack together all the seismograms within 1.5° of each individual reflection point at the CMB. The results obtained after this moving window averaging are presented in Fig. 6 (left column). Through the stacking, the local effects cancel out and the robust ones are averaged. The stacking clearly confirms and highlights the trends of the $\delta t^{\star}_{ScS-S}$ with epicentral distance (Fig. 6, middle column). As these values are used for an inversion in the following section, the contributions using PREM are not subtracted. The maps (left column) are more homogeneous but still display lateral variations. They are only partly explained by the variations in epicentral distance and are mostly related to lateral variations of intrinsic attenuation. However, these maps cannot be directly interpreted in terms of local attenuation anomalies near the CMB but represent an integrated and differential signal. It is therefore difficult to precisely locate the attenuation heterogeneities that would explain these maps.

In order to provide additional constraints on the origin of these $\delta t^{\star}_{ScS-S}$ anomalies, we also measure the elastic delay times δt_{ScS-S} between the S and the ScS. This is done by extracting the S and ScS signals filtered between 0.018 and 0.2 Hz, tapering them, correcting them for the effect of dispersion (using the attenuation

operator Eq. (2)) and of anisotropy and correlating the obtained waveforms. The elastic delay times are in good agreement with the predictions computed in the elastic 3-D model SAW24B16 (Mégnin and Romanowicz, 2000). We then average the time delays within the same 1.5°. They are plotted as a function of the $\delta t^{\star}_{ScS-S}$ in the right column of Fig. 6. Both $\delta t^{\star}_{ScS-S}$ and δt_{ScS-S} are corrected using PREM and SAW24B16. Because thermal activation of the intrinsic attenuation is usually assumed (e.g. Matas and Bukowinski, 2007), Q_{μ} depends more strongly on temperature than the elastic velocity. Correlation or anti-correlation between differential anelastic and elastic delay times could thus help to discriminate between thermal and compositional origin of the observed attenuation anomalies. The plots in Fig. 6 do not show a clear correlation. This suggests a complex compositional-thermal origin for the observed attenuation anomalies or effects like focusing or diffraction by small scale heterogeneities.

5. Radial variations

Although our dataset samples the mantle only in a few selected regions, we can invert our measurements in order to obtain a local 1-D Q_{μ} profile and compare with previous models. We use the $\delta t^{\star}_{ScS-S}$ obtained from stacks of seismograms. The inverse problem is solved using a least-square method (Tarantola and Valette, 1982) where we try both to explain the data within their uncertainties and remain close enough to an *a priori* attenuation model. We define depth dependent sensitivity kernels $K_i(r)$ associated with each observable i (in our case each $\delta t^{\star}_{ScS-S}$), such that

$$\delta t^{*}_{ScS-S,i} = \int K_i(r) \exp(\tilde{q}_{\mu}(r)) \, dr, \tag{3}$$

where $\tilde{q}_{\mu} = \ln(1000/Q_{\mu})$ is the parameter to be inverted for. The amplitude of $K_i(r)$, thus, represents the sensitivity of the i-th
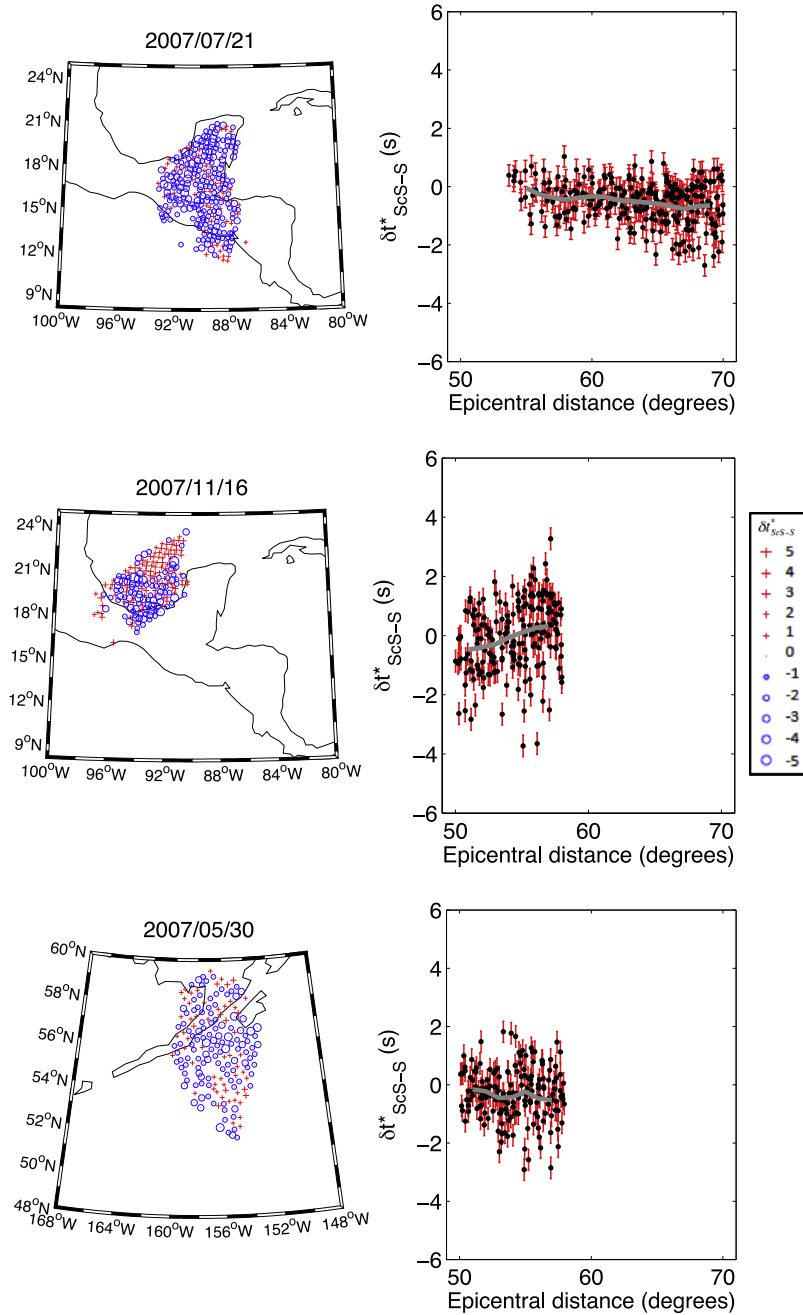
Fig. 5. Individual anelastic delay times. Measurements at the reflection point of the ScS on the CMB under Central America (top and middle) and under Alaska (bottom) for the three events considered in this study (see Fig. 4). The delays are corrected using PREM attenuation and the velocity model SAW24B16 (Mégnin and Romanowicz, 2000). (left column) Maps of the measured $\delta t_{ScS-S}^{\star}$ plotted at the reflection point of the ScS on the CMB. (right column) $\delta t_{ScS-S}^{\star}$ versus epicentral distances. The thick grey line represents the mean value. (For interpretation of the references to color in this figure caption, the reader is referred to the web version of this article.)

measurement to the attenuation at radius r. The computed sensitivity kernels, $K(r)$, computed using ray theory, for the whole dataset, are shown in Fig. 7. It confirms that the differential measurements are only marginally sensitive to the attenuation of the upper mantle and the transition zone. In the upper part of the lower mantle, near the bottoming depth for the S ray path, the sensitivity becomes maximum. Below the turning point, the kernels change sign. Decreasing the attenuation in the bottom of the lower mantle (i.e. decreasing the attenuation seen by the ScS only) or increasing it near its top (i.e. increasing the attenuation preferentially for the S) has a similar effect. Fig. 7 clearly illustrates that negative δt_{ScS-S}^{*} can only be obtained by increasing the attenuation close to the turning point of the S wave and, inversely, that positive δt_{ScS-S}^{*} can only be obtained by increasing the

attenuation in the lowermost mantle along the ScS path. The sensitivity of the $\delta t_{ScS-S}^{\star}$ is larger in the mid-mantle than in the D" layer. Moreover, as the epicentral distance increases (from blue to red in Fig. 7), the values of $\delta t_{ScS-S}^{\star}$ become sensitive to deeper regions: the maximum sensitivity is shifted by 1000 km between the epicentral distances of 50° and 70°.

In order to optimize the inversion procedure, we perform several tests. We introduce a correlation length L between two depths z_i and z_j by defining the *a priori* covariance matrix of the parameters as

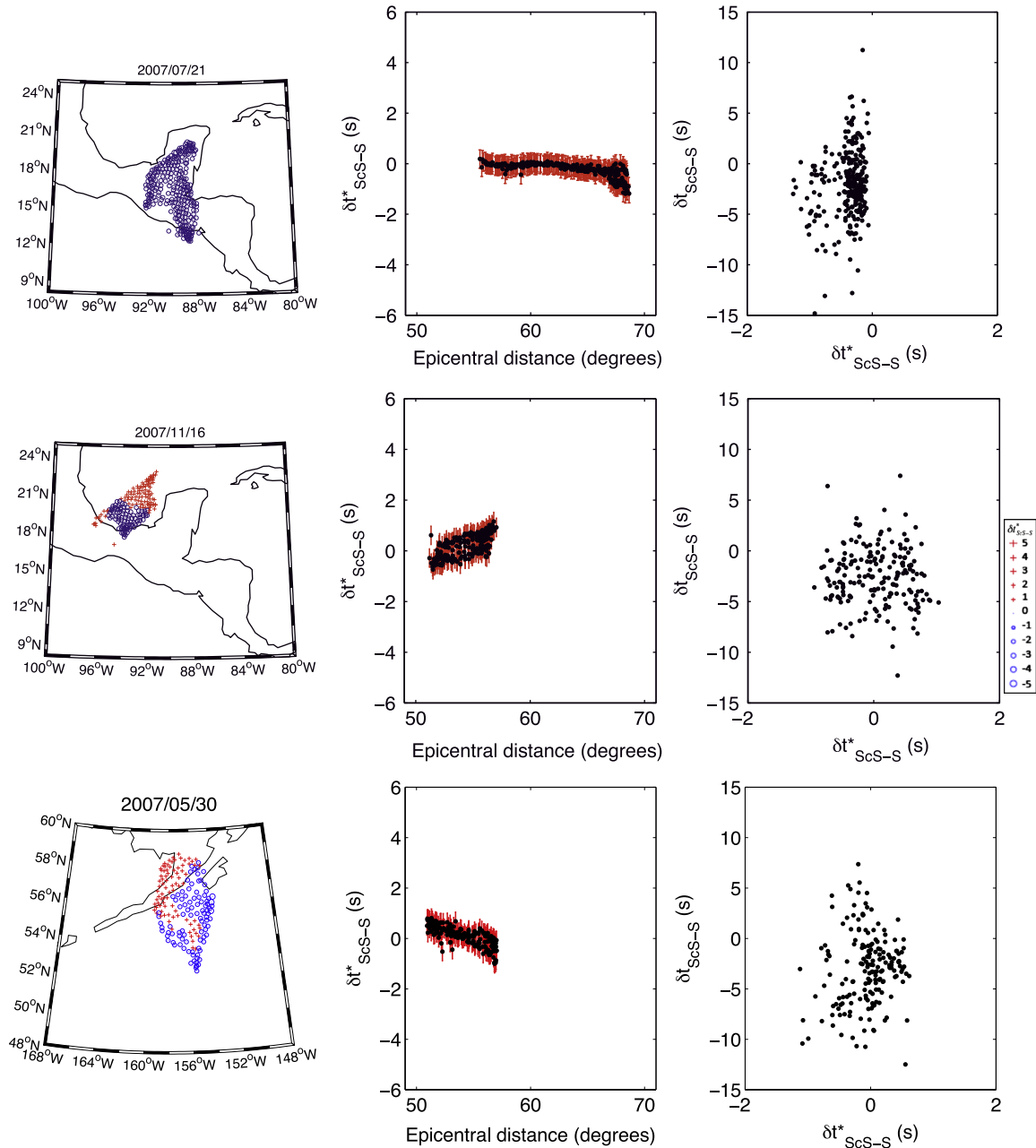$$C_p(i,j) = \sigma_m^2 \exp\left[-\frac{(z_i - z_j)^2}{2L^2}\right].$$

$$(4)$$

Fig. 6. Stacked anelastic delay times. (left column) Measurements plotted at the reflection point of the ScS on the CMB. (middle column) Measured δt^*_{ScS-S} versus epicentral distance. (right column) Elastic delay-times δt_{ScS-S} versus anelastic delay-times δt^*_{ScS-S}. Both quantities have been corrected using PREM and SAW24B16 for the propagation. The stacking highlights the revealed trends of the δt^*_{ScS-S} with the epicentral distance. No clear correlation is found between elastic and anelastic delay times.

We run the inversion procedure for various correlation lengths, L, and model uncertainties σ_m. As a priori information on the attenuation structure, we use the shear attenuation model QL6 of Durek and Ekström (1996) which is a better attenuation model than PREM for the lithosphere and the shallow layers. Since we have shown that the sensitivity kernels in the lithosphere are close to zero, we fix the value of Q_μ in the first 400 km to that of QL6. As always in inversions there is a trade-off between the fit to the observations and the distance to the a priori model. The tests lead to a classical "L-curve" variation of the data misfit as a function of the model uncertainty. A value $\sigma_m = 0.2$ appears to be reasonable whatever the correlation length chosen. Indeed, for greater σ_m the attenuation model is farther from QL6 without improving the data fit significantly.

We inverted various Q_μ models, separately for the two sampled regions (Fig. 8, grey curves) and for the whole dataset (Fig. 8, black

curves). We use a correlation length of 500 km. The data at short epicentral distance for Central America, with their large uncertainty, do not really constrain the inversion. The data from Alaska (AL) and for Central America (CA) at large epicentral distance, both require similar Q_μ profiles. The resulting Q_μ profile for the whole dataset (Table 1) is characterized by a maximum of attenuation in the mid-lower mantle ($Q_\mu \approx 250$). At the top of the lower mantle $Q_\mu \approx 300$ whereas at the CMB attenuation is rather low, with $Q_\mu \approx 450$. Compared to the other radial models depicted in Fig. 8, the trend of our regional model with depth is similar to that of QLM9 (Lawrence and Wysession, 2006a) but with 15% lower quality factor. The model of Hwang and Ritsema (2011) has a much lower attenuation than all other models. They do not use a differential measurement between two phases, S and ScS, recorded on the same seismogram but between two S phases recorded by two seismograms. This may make their approach less robust. However, the three
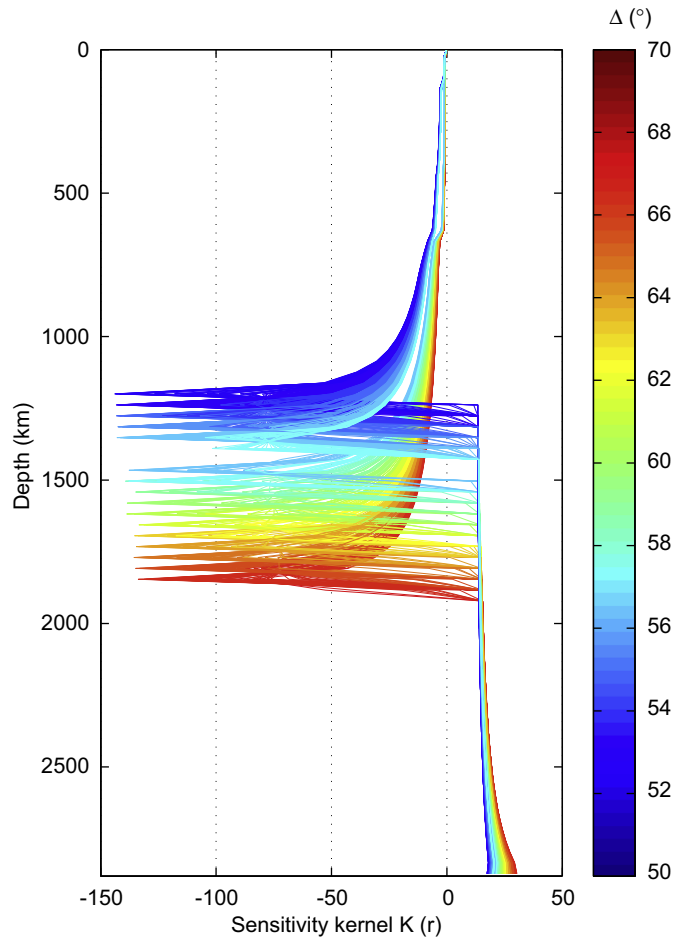
Fig. 7. Anelastic delay time sensitivity kernels. The colorbar indicates the epicentral distance. The sensibility is maximum and negative at the location of the turning points of the S wave while the sensibility is positive and somewhat reduced at the base of the mantle. It also shows that differential anelastic delay times are not sensitive to the attenuation structure of the lithosphere. (For interpretation of the references to color in this figure caption, the reader is referred to the web version of this article.)

Fig. 8. Various radial Q_μ models in the mantle. Our models (grey and black lines, CA for Central America and AL for Alaska) bear some similarities with the other body wave based models (red and blue curves) with a less attenuating bottom part of the lower mantle where the normal mode based models are more uniform. (For interpretation of the references to color in this figure caption, the reader is referred to the web version of this article.)

models based on body waves measurements: QLM9, that of Hwang and Ritsema (2011) and our model, all agree with a minimum of attenuation in the deep mantle. This increase in quality factor may be expected based on the significant increase in pressure in relation to the fairly flat adiabat, such that the homologous temperature drops continuously across the lower mantle. However, this is in contradiction with the Q_μ models deduced from the inversion of normal modes and surface wave attenuation data which suggest a lower mantle with uniform attenuation, although normal mode data may not have sufficient resolution to detect variations of Q with depth in the lower mantle.

Attenuation and viscosity are two anelastic responses of the mantle to deformation. Although the microscopic processes that lead to these responses might be totally different as they occur in very different frequency ranges, they are both thermally activated and thus some similarities between attenuation and viscosity profiles should be expected. The viscosity profiles of the deep mantle are unfortunately not much better constrained than those of attenuation. Some viscosity profiles are in agreement with our attenuation results, having a minimum in the mid-lower mantle (Kaufmann and Lambeck, 2000; Forte and Mitrovica, 2001), but others have found a broad viscosity maximum through the lower mantle (Ricard and Wuming, 1991; Corrieu et al., 1995; Mitrovica and Forte, 2004).

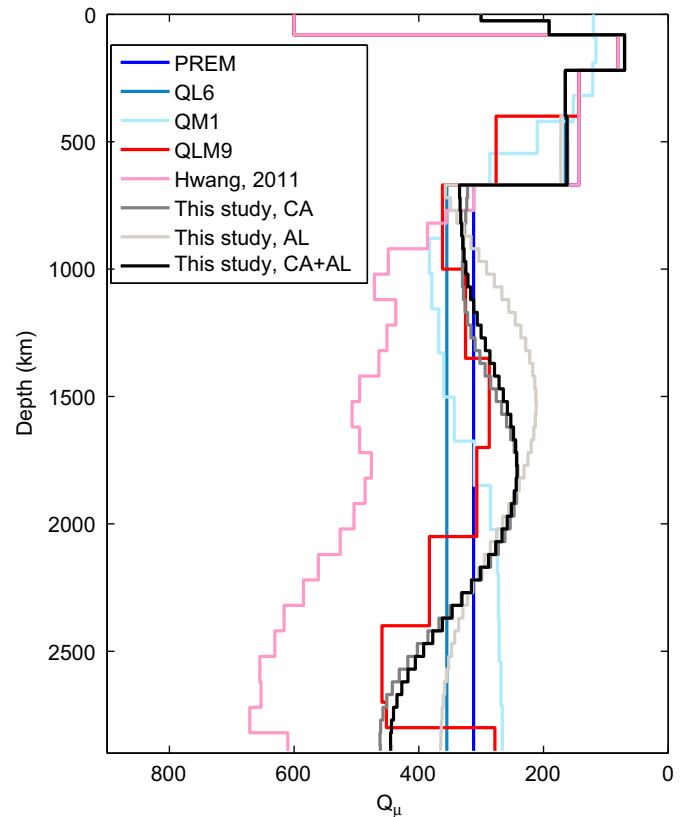The discrepancy of our model with the low frequency Q_μ models might be related to the fact that our data sample lower

mantle regions where slab material has been injected and has been detected by seismic tomography (e.g. Hutko et al., 2006; Ren et al., 2007). A low attenuation in the abyssal mantle could be related to the presence of cold slabs ponding on the CMB. The existence of an attenuation maximum in the mid-lower mantle has also been observed by Lawrence and Wysession (2006a). The quality factors that we infer in the lowest mantle are on average larger than in PREM. This might also be due to a frequency dependence of the attenuation. Indeed various authors have suggested that $Q_\mu \propto \omega^\alpha$ with $\alpha \approx 0.1$–0.6 both from seismic (Dziewonski and Anderson, 1981; Choy and Cormier, 1986; Ulug and Berckhemer, 1984; Oki et al., 2000; Warren and Shearer, 2000, 2002; Shito et al., 2004; Lekic et al., 2009) and mineralogical studies (Karato and Spetzler, 1990; Jackson et al., 2005). Considering that the attenuation in PREM is mostly constrained by seismic observations at frequencies ≈ 50 times lower than those of body waves, we can explain that our Q_μ values are $\approx 45\%$ larger than in PREM in the deep mantle ($Q_\mu \approx 450$ in our study instead of $Q_\mu \approx 312$ in PREM) with a low value of $\alpha = 0.1$. However, with the same correction, it may be more difficult to reconcile the attenuation values in the upper part of the lower mantle. At the same time, the upper part of the lower mantle may have been constrained in PREM by higher frequency modes, approaching, thus, the frequencies used in our studies. This would explain that the differences between our model and PREM increase with depth in the lower mantle (Oki and Shearer, 2008).

To illustrate the fit to the observations, Fig. 9 depicts the $\delta t^\star_{ScS-S}$ variations with epicentral distance, computed for various attenuation models and for our model. We computed the $\delta t^\star_{ScS-S}$ for a deep earthquake (a source located at the depth of 600 km). For our

Table 1
Best-fitting Q_μ model.

Layer	Depth (km)	Q_μ
1	0–25	300
2	25–80	191
3	80–220	70
4	220–400	165
5	400–450	162.4
6	450–500	162.3
7	500–550	162.3
8	550–600	162.3
9	600–670	162.3
10	670–720	334.6
11	720–770	333.7
12	770–820	332.6
13	820–870	331.2
14	870–920	329.5
15	920–970	327.3
16	970–1020	324.5
17	1020–1070	321.1
18	1070–1120	316.9
19	1120–1170	311.9
20	1170–1220	306.3
21	1220–1270	299.9
22	1270–1320	293.1
23	1320–1370	285.9
24	1370–1420	278.5
25	1420–1470	271.2
26	1470–1520	264.3
27	1520–1570	258.0
28	1570–1620	252.4
29	1620–1670	247.9
30	1670–1720	244.7
31	1720–1770	242.8
32	1770–1820	242.4
33	1820–1870	243.7
34	1870–1920	246.7
35	1920–1970	251.5
36	1970–2020	258.1
37	2020–2070	266.5
38	2070–2120	276.5
39	2120–2170	288.2
40	2170–2220	301.3
41	2220–2270	315.6
42	2270–2320	330.7
43	2320–2370	346.4
44	2370–2420	362.1
45	2420–2470	377.5
46	2470–2520	392.1
47	2520–2570	405.5
48	2570–2620	417.3
49	2620–2670	427.1
50	2670–2720	434.9
51	2720–2770	440.4
52	2770–2820	443.8
53	2820–2870	445.2
54	2870–2891	444.9

Correlation length: 500 km

Fig. 9. Anelastic delay times computed for various Q_μ models. The $\delta t^\star_{ScS-S}$ are computed using Eq. (2), and considering a deep source, located at the depth of 600 km (full lines). For comparison, in the case of our regional model we also calculate for a shallow source, located at the depth of 150 km (dashed line). The measurements shown in Fig. 5 are also reported (circles, squares and diamonds, CA for Central America and AL for Alaska).

The predictions of PREM and QL6 models do not fit the data trend at epicentral distances above 55°. The QM1 model seems to be incompatible with our anelastic delay times.

6. Conclusions

In this study, we apply the method proposed by Ford et al. (2012), based on instantaneous frequency matching, in order to obtain ScS–S differential anelastic delay times, $\delta t^\star_{ScS-S}$. We illustrate that the IFM method is more robust than the SR method. By carefully analyzing the effects of noise, source mechanism and phase interference, we show that the data must be rigorously selected in order to yield accurate results. Our study confirms the difficulty to obtain robust and reliable observations of mantle attenuation. The necessary strict selection procedure makes it difficult to obtain values of the $\delta t^\star_{ScS-S}$ with a systematic and automated procedure, particularly when the SR method is used.

Using an additional stacking procedure, we were able to highlight a clear dependence of the anelastic delay time with epicentral distance, in spite of the limited number of data. The absence of correlation between the anelastic and elastic delay-times also indicates a likely compositional origin for the attenuation anomalies although effects of scattering by small scale heterogeneities in the lower mantle cannot be ruled out. The 1-D inversion indicates a non-uniform lower mantle attenuation structure with the presence of an attenuating zone in the mid-lower mantle and a lower attenuation at its base. Our 1-D model agrees with the fact that the abyssal mantle seems less attenuating with body waves than with normal modes. However, our data sample two specific regions beneath subduction zones, so part of the discrepancy may be due to large scale lateral variations in Q. The disagreement between high-frequency and low-frequency based radial attenuation models, often pointed in the literature may only partly be solved by a frequency dependent attenuation with $Q_\mu \propto \omega^\alpha$ with $\alpha = 0.1$–0.2.

model we also considered the case of a shallow earthquake (150 km deep, denoted by the dashed black line). When the epicentral distance increases, the S ray becomes closer to the ScS ray and the $\delta t^\star_{ScS-S}$ tends to zero (for an event depth of 600 km, S and ScS paths coincide around 100° of epicentral distance). This is why our $\delta t^\star_{ScS-S}$ predictions increase after 70°, even though we have no data in this domain. As discussed previously, the three models based on body waves have common features. However, our regional model displays a stronger decrease of anelastic delay times with epicentral distance than that obtained by Lawrence and Wysession (2006a) and Hwang and Ritsema (2011).
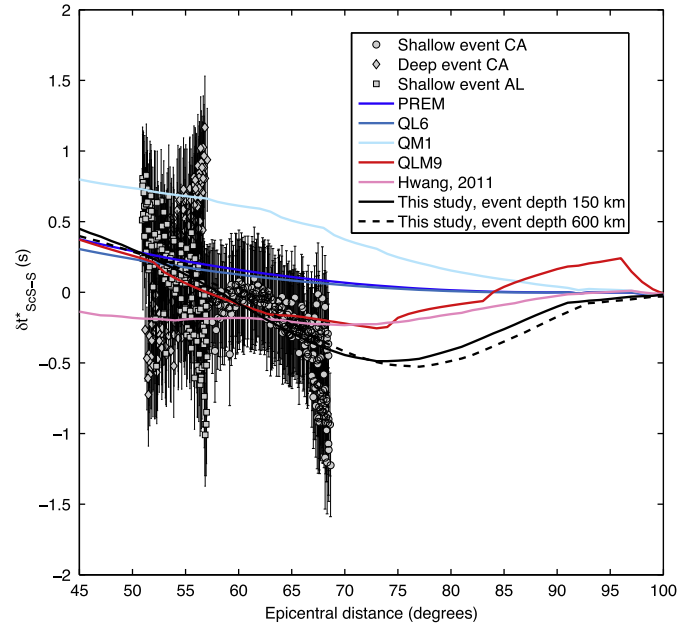
Acknowledgments

References

Aki, K., Richards, P., 1980. Quantitative Seismology, Theory and Methods. Freeman and Co., New York.

Anderson, Don L., 1980. Bulk attenuation in the Earth and viscosity of the core. Nature 285, 204–207.

Bhattacharyya, J., 1998. Comparison between time-domain and frequency-domain measurement techniques for mantle shear-wave attenuation. Pure Appl. Geophys. 153, 399–417.

Chan, W.W., Der, Z.A., 1988. Attenuation of multiple ScS in various parts of the world. Geophys. J. 92, 303–314.

Choy, G.L., Cormier, V.F., 1986. Direct measurement of the mantle attenuation operator from broadband P and S waves. J. Geophys. Res. 91, 7326–7342.

Corrieu, V., Thoraval, C., Ricard, Y., 1995. Mantle dynamics and geoid Green functions. Geophys. J. Int. 120, 516–523.

Durek, J.J., Ekström, G., 1995. Evidence of bulk attenuation in the asthenosphere from recordings of the Bolivia earthquake. J. Geophys. Res. 22, 2309–2312.

Durek, J.J., Ekström, G., 1996. A radial model of anelasticity consistent with long-period surface wave attenuation. Bull. Seismol. Soc. Am. 86, 144–158.

Dziewonski, A.M., Anderson, D.l., 1981. Preliminary reference Earth model. Phys. Earth Planet. Inter. 25, 297–356.

Forte, A.M., Mitrovica, J.X., 2001. Deep-mantle high-viscosity flow and thermo-chemical structure inferred from seismic and geodynamic data. Nature 410, 1049–1056.

Ford, S.R., Garnero, E.J., Thorne, M.S., 2012. Differential t* measurements via instantaneous frequency matching: observations of lower mantle shear attenuation heterogeneity beneath western Central America, Geophys. J. Int.,189, pages 513–523.

Fuchs, K., Müller, G., 1971. Computation of synthetic seimograms with the reflectivity method and comparison with observations. Geophys. J. R. Astron. Soc. 23, 417–433.

Hutko, A.R., Lay, T., Garnero, E.G., Revenaugh, J., 2006. Seismic detection of folded, subducted lithosphere at the core–mantle boundary. Nature 441, 333–336.

Hwang, Y.K., Ritsema, J., 2011. Radial Q_μ structure of the lower mantle from teleseismic body-wave spectra. Earth Planet. Sci. Lett. 303, 369–375.

Jackson, D.D., Anderson, D.L., 1970. Physical mechanisms of seismic-wave attenuation. Rev. Geophys. 8, 1–63.

Jackson, I., Webb, S., Weston, L., Boness, D., 2005. Frequency dependence of elastic wave speeds at high temperature: a direct experimental demonstration. Phys. Earth Planet. Inter. 148, 8596.

Jordan, T.H., Sipkin, S.A., 1977. Estimation of the attenuation operator for multiple ScS waves. Geophys. Res. Lett. 4, 167–170.

Karato, S., Spetzler, H.A., 1990. Defect microdynamics in minerals and solids-state mechanisms of seismic wave attenuation and velocity dispersion in the mantle. Rev. Geophys. 28, 399–421.

Karato, S.-I., Karki, B.B., 2001. Origin of lateral variation of seismic wave velocities and density in the deep mantle. J. Geophys. Res. 106, 21771–21783.

Kaufmann, G., Lambeck, K., 2000. Mantle dynamics, postglacial rebound and radial viscosity profile. Phys. Earth Planet. Inter. 121, 301–324.

Kendall, J-M., Silver, P.G., 1996. Constraints from seismic anisotropy on the nature of the lowermost mantle. Nature 381, 409–412.

Lawrence, J.F., Wysession, M.E., 2006a. QLM9: a new radial quality factor (Q_μ) model for the lower mantle. Earth Planet. Sci. Lett. 241, 962–971.

Lay, T., Wallace, T.C., 1983. Multiple ScS travel times and attenuation beneath Mexico and Central America. Geophys. Res. Lett. 10, 301–304.

Lekic, V., Matas, J., Panning, M., Romanowicz, B., 2009. Measurement and implications of frequency dependence of attenuation. Earth Planet. Sci. Lett. 282, 285–293.

Matas, J., Bukowinski, M.S.T., 2007. On the anelastic contribution to the temperature dependence of lower mantle seismic velocities. Earth Planet. Sci. Lett., 259, 51–65.

Matheney, M.P., Nowack, R.L., 1995. Seismic attenuation values obtained from instantaneous-frequency matching and spectral ratios. Geophys. J. Int. 123, 1–15.

Masters, G., Laske, G., Bolton, H., Dziewonski, A., 2000. The relative behavior of shear velocity, bulk sound speed, and compressional velocity in the mantle: implications for chemical and thermal structure. Geophys. Monogr. 117, 63–88.

Mégnin, C., Romanowicz, B., 2000. The shear velocity structure of the mantle from the inversion of body, surface and higher modes waveforms. Geophys. J. Int. 143, 709–728.

Mitrovica, J.X., Forte, A.M., 2004. A new inference of mantle viscosity based upon joint inversion of convection and glacial isostatic adjustment data. Earth Planet. Sci. Lett. 225, 177–189.

Müller, G., 1983. Rheological properties and velocity dispersion of a medium with power-law dependence of Q on frequency. J. Geophys. 54, 20–29.

Müller, G., 1985. The reflectivity method: a tutorial. J. Geophys. 58, 153–174.

Nakanishi, I., 1979. Attenuation of multiple ScS waves beneath the Japanese arc. Phys. Earth Planet. Inter. 19, 337–347.

Nowacki, A., Wookey, J., Kendall, J.-M., 2010. Deformation of the lowermost mantle from seismic anisotropy. Nature 467, 1091–1095.

Oki, S., Fukao, Y., Obayashi, M., 2000. Reference frequency of teleseismic body waves. J. Geophys. Res. 109 http://dx.doi.org/10.1029/2003JB002821.

Oki, S., Shearer, P.M., 2008. Mantle Q structure from S–P differential attenuation measurements. J. Geophys. Res. 113, B12308, http://dx.doi.org/10.1029/2007JB005567.

Resovsky, J.S., Trampert, J., Van der Hilst, R.D., 2005. Error bars for the global seismic Q profile. Earth Planet. Sci. Lett. 230, 413–423.

Ricard, Y., Wuming, B., 1991. Inferring the viscosity and the 3-D density structure of the mantle from geoid, topography and plate velocities. Geophys. J. Int. 105, 561–571.

Ricard, Y., Mattern, E. and Matas, J., 2005, Mineral physics in thermo-chemical mantle models, In: Hilst, R., Bass, J.D., Matas, Trampert, J., (Eds.), Com-position, Structure and Evolution of the Earth Mantle, AGU monograph, vol. 160, pp. 283–300.

Romanowicz, B., Durek, J., 2000. Seismological constraints on attenuation in the earth: a review. In: Karato, S., et al. (Eds.), Earth's Deep Interior: Mineral Physics and Tomography from the Atomic to the Global Scale, AGU Monograph, vol. 117, pp. 161–180.

Romanowicz, B., Mitchell, B., 2007. Q of the Earth from crust to core. In: Treatise of Geophysics, vol. 1, Elsevier, pp. 731–774.

Ren, Y., Stutzmann, E., Van Der Hilst, R.D., Besse, J., 2007. Understanding seismic heterogeneities in the lower mantle beneath the Americas from seismic tomography and plate tectonic history. J. Geophys. Res. 112, B01302.

Shito, A., Karato, S., Park, J., 2004. Frequency dependence of Q in the Earth's upper mantle inferred from continuous spectra of body waves. Geophys. Res. Lett. 31, 582, http://dx.doi.org/10.1029/2004GL019.

Silver, P.G., Chan, W.W., 1991. Shear wave splitting and subcontinental mantle deformation. J. Geophys. Res. 96, 16429–16454.

Sipkin, S.A., Jordan, T.H., 1980. Regional variations of Q_{ScS}. Bull. Seismol. Soc. Am. 70, 1071–1102.

Sipkin, S.A., Revenaugh, J., 1994. Regional variations of attenuation and travel time in China from analysis of multiple-ScS phases. J. Geophys. Res. 99, 2687–2699.

Suetsugu, D., 2001. A low Q_{ScS} anomaly near the South Pacific Superswell. Geophys. Res. Lett. 28, 391–394.

Tarantola, A., Valette, B., 1982. Generalized nonlinear inverse problems solved using the least squares criterion. Rev. Geophys. Space Phys. 2, 219–232.

Taner, M.T., Koehler, F., Sheriff, R.E., 1979. Complex seismic trace analysis. Geophysics 44, 1041–1063.

Trampert, J., Deschamps, F., Resovsky, J., Yuen, D.A., 2004. Probabilistic tomography maps chemical heterogenities throughout the mantle. Science 306, 853–856.

Ulug, A., Berckhemer, G., 1984. Frequency dependence of Q for seismic body waves in the Earth's mantle. J. Geophys. 56, 9–19.

Warren, L.M., Shearer, P.M., 2000. Investigating the frequency dependence of mantle Q by stacking P and PP spectra. J. Geophys. Res. 105, 25391–25402.

Warren, L.M., Shearer, P.M., 2002. Mapping lateral variations in upper mantle attenuation by stacking P and PP spectra. J. Geophys. Res. 107 http://dx.doi.org/10.1029/2001JB001195.

Widmer, R., Masters, G., Gilbert, F., 1991. Spherically symmetric attenuation within the Earth from normal mode data. Geophys. J. Int. 104, 541–553.

Wüstefeld, A., Bokelmann, G., Zaroli, C., Barruol, G., 2008. SplitLab: a shear-wave splitting environment in Matlab. Comput. Geosci. 344, 515–528.

Zaroli, C., Debayle, E., Sambridge, M, 2010. Frequency-dependent effects on global S-wave traveltimes: wavefront-healing, scattering and attenuation. Geophys. J. Int. 182, 1025–1042.